Industrial Chemistry & Materials

ROYAL SOCIETY OF CHEMISTRY

PAPER

View Article Online
View Journal | View Issue

Cite this: *Ind. Chem. Mater.*, 2025, **3**, 87

Copper ions-intercalated manganese dioxide self-supporting mesoporous carbon electrode for aqueous zinc-ion batteries†

Richeng Jin, Yuan Fang, Beibei Gao, Ying Wan, Yi Zhou, Guofeng Rui, Wei Sun,* Pengpeng Qiu* and Wei Luo *

In aqueous zinc-ion batteries (AZIB), layered manganese dioxide (δ-MnO_2) is considered to be a suitable cathode material due to its high theoretical capacity, suitable operating voltage and Zn^{2+}/H^+ co-intercalation mechanism. However, the strong coulomb interaction between Zn^{2+} and δ-MnO_2 results in the slow diffusion dynamics of Zn^{2+} in the electrochemical process, which affects the structural stability of the cathode. Herein, we report a structural design that stabilizes the δ-MnO_2-layered structure by pre-intercalation of Cu^{2+} to expand the layer spacing, and thus improve H^+-transfer kinetics. Compared with the bulk δ-MnO_2, the modified cathode showed excellent electrochemical performances, including a highly reversible capacity of 280 mA h g^{-1} at 1 A g^{-1} and 62.5% capacity retention after 1500 cycles at 5 A g^{-1}. The results shown above confirmed the possibility of increasing the capacity contribution of H^+ through structural design, and provides a novel idea for the development of high-performance cathode materials.

Received 22nd April 2024,
Accepted 30th May 2024

DOI: 10.1039/d4im00042k

rsc.li/icm

Keywords: Aqueous zinc-ion batteries; Layered manganese dioxide; Pre-intercalation; Self-supporting electrode.

1 Introduction

The excessive consumption of traditional fossil fuels has led to the development of reliable and low-cost electrochemical energy storage systems (EESs). The latter are used to attain a wide application of clean energies such as nuclear and geothermal energy.[1–7] Aqueous Zn-ion batteries (AZIB) with a suitable redox potential (−0.76 V *vs.* standard hydrogen electrode) and large specific capacity (820 mA h g^{-1}) are considered to be promising EESs due to their advantages of low cost, safety, and non-toxicity.[8–10] However, the structural phase transition of the cathode and dissolution of the active substance limit the whole performance of ZIB.[11,12] Therefore, the exploration of a suitable cathode material is particularly important for the commercialization of AZIB.

Manganese-based oxides, vanadium-based oxides, Prussian blue analogues, and organic compounds have been extensively studied.[13–17] Among them, manganese oxide has attracted tremendous interest because of its high specific capacity of ~308 mA h g^{-1}, large operating voltage of ~1.35 V, and low toxicity. Compared with the other phases of MnO_2 (α-, β-, γ-, ε-, λ-MnO_2), the layered structure of δ-MnO_2 has a large layer spacing (~0.7 nm), which makes it theoretically more suitable for the intercalation of Zn ions.[18–20] However, δ-MnO_2 still has the problems of poor kinetics of ion diffusion and unstable structure, which lead to poor magnification performance and rapid capacity decay in practical applications. To address these problems, pre-intercalation,[21] oxygen defects,[22] structural design,[23] and construction of composite materials[24] are usually employed to boost the electrochemical properties of the cathode. In particular, the pre-intercalation strategy is of great importance because it can increase the conductivity of MnO_2 and expand the lattice spacing to improve the ion-transport dynamics. For example, Zhang *et al.* prepared a PVP-intercalated layered manganese dioxide by a hydrothermal method. It showed a high performance for Zn-ion storage by accelerating electron and interlayer ion transport.[25] Jing *et al.* reported a dual-ion intercalation strategy to incorporate Mg^{2+} and K^+ into δ-MnO_2, which showed high stability during an electrochemical process.[21] The above studies show that the pre-intercalation of different ions affects the contribution ratio of H^+ and Zn^{2+}. However, Zn^{2+} has a strong electrostatic interaction with the base material, resulting in slow kinetics,

State Key Laboratory for Modification of Chemical Fibers and Polymer Materials, College of Materials Science and Engineering, Institute of Functional Materials, Donghua University, Shanghai 201620, China. E-mail: weisun@dhu.edu.cn, qiupengpeng@dhu.edu.cn, wluo@dhu.edu.cn

† Electronic supplementary information (ESI) available. See DOI: https://doi.org/10.1039/d4im00042k

while H^+ has faster reaction kinetics and weak interaction with the main structure. Hence, it is a practicable scheme to increase the capacity contribution of H^+.

Herein, we prepared a Cu^{2+}-intercalated MnO_2 self-supporting electrode as the cathode of AZIB. In order to improve the intrinsic low wettability of the original carbon cloth, mesoporous structures were constructed *in situ* on the carbon cloth to provide a 'cradle' for the growth of δ-MnO_2. Then, Cu^{2+}-intercalated δ-MnO_2 was grown on the substrate by a hydrothermal method. The Cu^{2+} intercalation greatly expanded the lattice spacing and strengthened the diffusion kinetics of H^+ while maintaining the original layered structure. Benefiting from the superior structural design, the Cu–MnO_2 cathode delivered a high specific capacity and excellent cycling stability.

2 Results and discussion

Fig. 1 shows the synthetic scheme of the Cu–MnO_2 cathode. The polyethylene oxide-*b*-styrene (PEO-*b*-PS) copolymer template was first prepared by an atom-transfer radical-polymerization method.[26] Gel permeation chromatography of PEO-*b*-PS (Fig. S1†) showed that the molecular weight was 44 343.0 g mol^{-1} and the polydispersity index was ~1.0, indicating the high quality of PEO-*b*-PS. Then, mesoporous carbon layers were grown on both sides of the carbon cloths (CCs) through assembly of interfacial monomicelles, followed by a carbonization process in N_2. Finally, Cu ions-intercalated δ-MnO_2 was deposited on the surface of mesoporous carbon through a hydrothermal reaction.[27,28] As a comparison, δ-MnO_2 was prepared by a similar method without addition of the Cu precursor.

Field-emission scanning electron microscopy (FESEM) and high-resolution transmission electron microscopy (HRTEM) were used to observe the morphology and microstructure of samples. Compared with the original carbon cloth, mesoporous carbon structures were clearly deposited on the surface of the carbon cloth (Fig. S2a–d†). After hydrothermal treatment, Cu–MnO_2 nanosheets grew uniformly on the surface of the mesoporous carbon cloth with an ordered nanoarray morphology (Fig. 2a–c and S3a†). TEM images (Fig. 2d and e and S3b†) also show similar nanoarray structures with a width of 75 nm. Fig. 2e displays the high-resolution HRTEM of Cu–MnO_2, which clearly revealed a lamellar structure with a *d*-spacing of 0.75 nm which belongs to the (001) crystal plane of δ-MnO_2 (JCPDS no. 80-1098). The distinct diffraction rings in the SAED pattern showed that Cu^{2+} intercalation did not change the phase type of δ-MnO_2. However, compared with δ-MnO_2 (Fig. S3c†), the *d*-spacing of Cu–MnO_2 increased, which was caused by Cu^{2+} intercalation. Energy dispersive X-ray spectroscopy (EDX) (Fig. 2g) exhibited a uniform distribution of elements in Cu–MnO_2, indicating the average distribution of Cu^{2+} into δ-MnO_2.

The crystal structures of cathodes were examined by XRD. In the XRD patterns of δ-MnO_2, the diffraction peaks at 12°, 26.2°, and 37.5° correspond well to the (001), (002), and (−111) planes of δ-MnO_2 (JCPDS no. 80-1098), indicating the synthesis of layered manganese dioxide. Cu–MnO_2 showed a similar XRD pattern to that of δ-MnO_2, further indicating that the intercalation of Cu^{2+} did not break the phase structure of δ-MnO_2. Raman spectra of the cathodes (Fig. 3b) showed characteristic peaks at 500, 575 and 649 cm^{-1} belonging to the Mn–O–Mn stretching vibration, Mn–O vibration along the skeleton chain, and the symmetric stretching vibration Mn–O bond, respectively.[29,30] These data suggested that these two samples had a typical crystal structure of birnessite-type. In addition, the difference in relative intensity of the Raman band between the two samples reflected the species variation

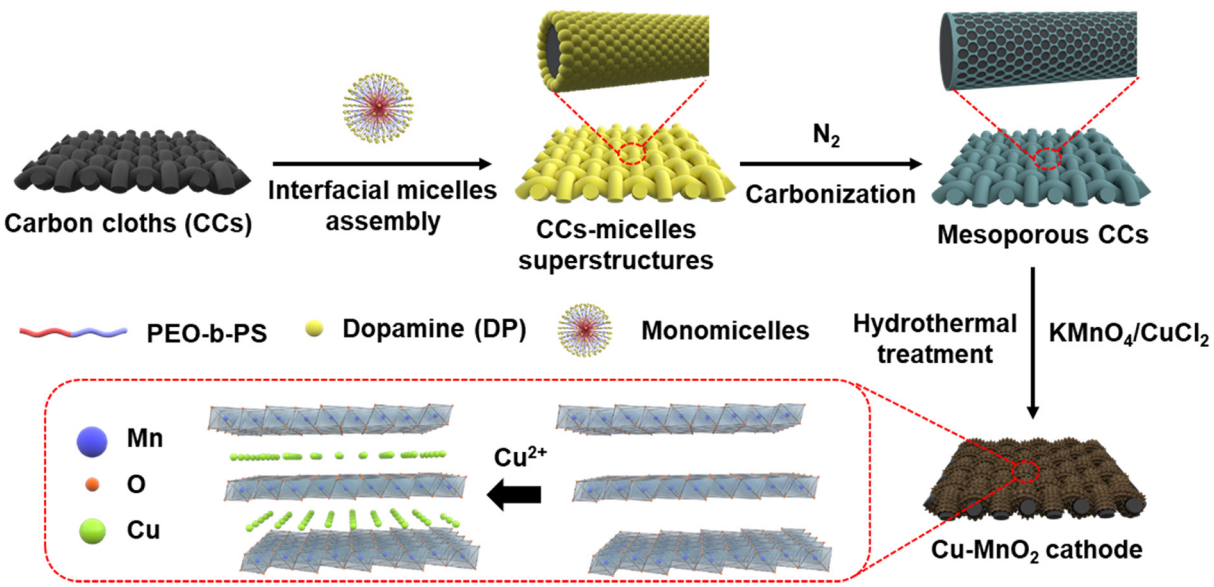

Fig. 1 Synthesis of Cu–MnO_2 (schematic).

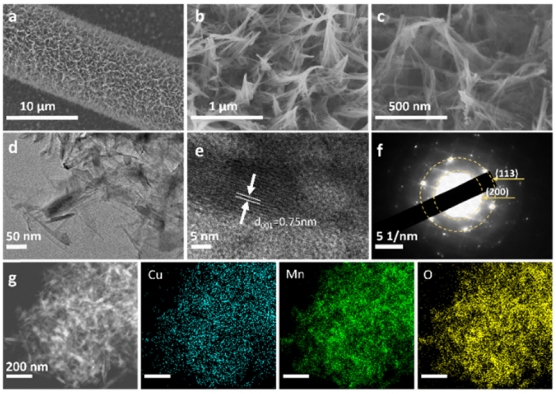

Fig. 2 (a–c) SEM images, (d) TEM image, (e) HRTEM image, (f) SAED pattern, and (g) HAADF-STEM image and corresponding elemental mapping images of Cu–MnO_2.

between layered δ-MnO_2 layers.[31] The N_2 sorption isotherms of Cu–MnO_2 exhibited a typical type-IV characteristic curve and a H3-type hysteresis loop, suggesting that Cu–MnO_2 had a mesoporous structure.[32,33] The Brunauer–Emmett–Teller (BET) surface area and pore size of Cu–MnO_2 were calculated to be 3.7 nm and 23.0 $m^2\ g^{-1}$, respectively. In order to determine the source of the mesoporous structure of the electrode, nitrogen absorption and desorption tests were carried out on the treated carbon cloth. As shown in Fig. S2c,† the treated carbon cloth had a mesoporous structure, and its specific surface area and pore size were 3.096 $m^2\ g^{-1}$ and 7.4 nm, respectively. This result showed that the mesoporous structure of the electrode was mainly derived from the accumulation of Cu–MnO_2 nanosheets rather than mesoporous carbon cloth. The elemental composition of Cu–MnO_2 was investigated by X-ray photoelectron spectroscopy (XPS). In the Mn 2p XPS spectrum of MnO_2 (Fig. 3d), dominant peaks of Mn 2p3/2 and Mn 2p1/2 were located at 642.4 and 654.3 eV, respectively. In the Mn 2p XPS spectrum of Cu–MnO_2, both Mn^{4+} and Mn^{3+} were present.[34] Among them, the amount of Mn^{4+} was 71.98% (Fig. S4b†) and the average chemical valence of Mn was +3.72. The valence state of Mn can be explained by the representative multiplet splitting caused by the exchange of electrons at its 3s–3d level.[35–37] As shown in Fig. 3e, the splitting energy (ΔE) of the two 3s peaks increased from 4.73 eV of δ-MnO_2 to 5.03 eV of Cu–MnO_2, indicating an increase in the amount of Mn^{3+} in order to balance the valence imbalance caused by Cu^{2+} intercalation. XPS of O 1s (Fig. 3f) showed lattice oxygen (O_{lat}) and O (O_{Mn-OH}) which belonged to Mn–OH.[34] We found that after pre-intercalation of Cu^{2+}, O_{lat} was transferred in a more negative direction so that O_{lat} had more electrons, which was due to electron transfer between the embedded Cu^{2+} and lattice oxygen. The increase in the charge around the O atom greatly strengthened the adsorption capacity of Cu–MnO_2 for H^+, improved the diffusion capacity of H^+, and more H^+ participated in the electrode reaction, thereby showing higher electrochemical performance. In Fig. S4,† characteristic peaks of Cu^{2+} were found at 934.3 eV and 954 eV, and belonged to Cu 2p 3/2 and Cu 2p 1/2, respectively. There were oscillating satellite peaks of Cu^{2+} at 942.7 eV and 962.4 eV, suggesting that Cu^{2+} had embedded within δ-MnO_2.

For research into the electrochemical properties of Cu–MnO_2, a coin cells configuration with a zinc anode, glass fiber film (Whatman, GF/D), and 2 M $ZnSO_4$ and 0.2 M

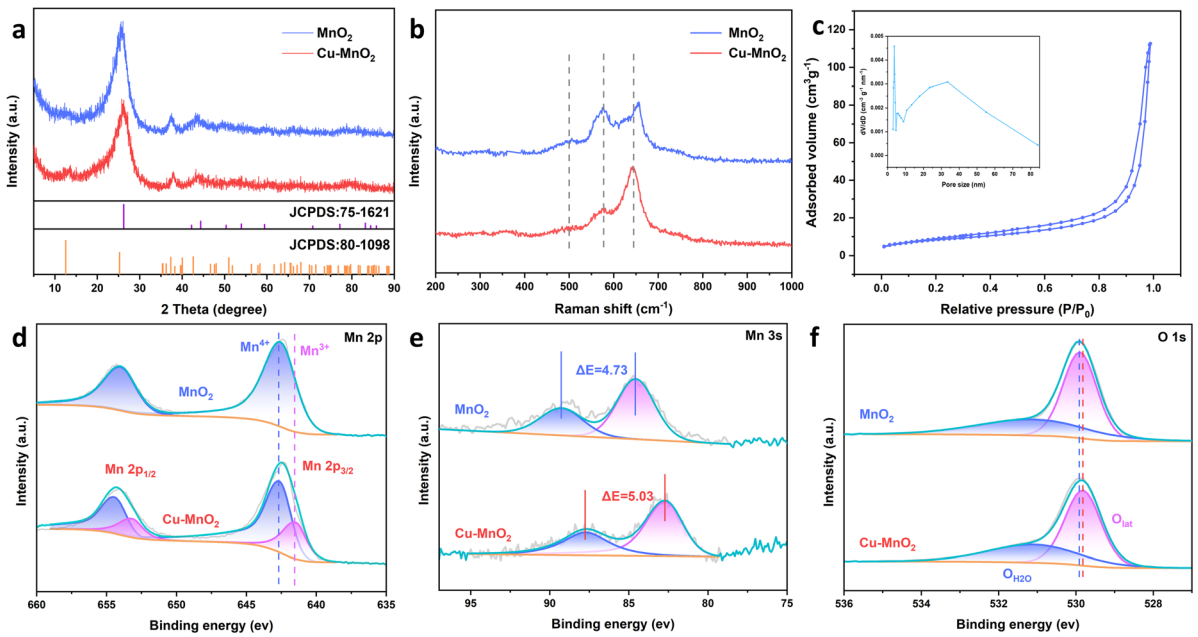

Fig. 3 (a) XRD curves, (b) Raman spectra, (c) N_2 sorption isothermals and pore-size distribution of Cu–MnO_2. (d) XPS spectra of Mn 2p. (e) XPS spectra of Mn 3s. (f) O 1s XPS spectra of Cu–MnO_2.

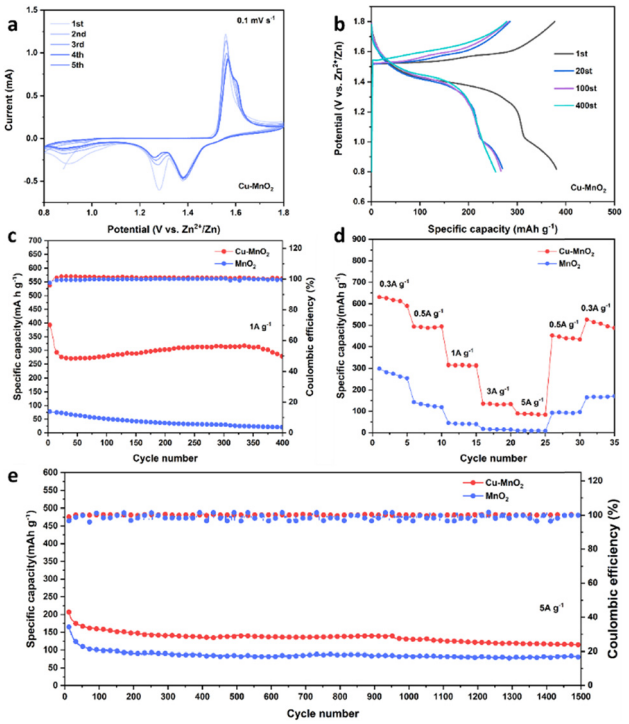

Fig. 4 (a) CV curves at 0.1 mV s^{-1}. (b) GCD curves at 1.0 A g^{-1} of Cu–MnO_2. (c) Cycling performance of Cu–MnO_2 and δ-MnO_2 at a current density of 1.0 A g^{-1}. (d) Rate performance for Cu–MnO_2 and δ-MnO_2. (e) Long-cycling performance at 5.0 A g^{-1}.

$MnSO_4$ as the electrolyte were employed. The addition of $MnSO_4$ can inhibit the dissolution of Mn^{2+} during discharge processes.[38,39] The cyclic voltammetry (CV) curves of Cu–MnO_2 and δ-MnO_2 at 0.1 mV s^{-1} are shown in Fig. 4a and S5a,† respectively. The two pairs of redox peaks of 1.56/1.38 V and 1.6/1.26 V corresponded to the deintercalation/intercalation of H^+ and Zn^{2+}, respectively. The almost overlapping CV curve after the first two cycles (Fig. 4a) illustrated the stable and reversible charge and discharge processes of the Cu–MnO_2 cathode material. At the same time, the larger CV area of Cu–MnO_2 compared with that of δ-MnO_2 also indicated that Cu–MnO_2 provided more capacity. The galvanostatic charge–discharge (GCD) voltage profiles of Cu–MnO_2 are shown in Fig. 4b, and display two charge–discharge platforms, which is consistent with CV curve. The reduction in capacity after the first cycle may have been due to the phase transition of Cu–MnO_2 caused by incomplete deintercalation/intercalation of Zn^{2+} in Cu–MnO_2. No obvious change of charge/discharge curves in subsequent cycles indicated that the Cu–MnO_2 electrode had excellent cyclic stability. The cycling performance of Cu–MnO_2 and δ-MnO_2 cathode under the rate of 1 A g^{-1} is shown in Fig. 4c. The Cu–MnO_2 cathode stabilized at 300 mA h g^{-1} after the initial capacity reduction, and was maintained at 280 mA h g^{-1} after 400 cycles, with a capacity attenuation rate of 7%. By comparison, the δ-MnO_2 cathode exhibited poor cyclic performance, with 70% capacity fading after 400 cycles. It is worth noting that an increase in capacity was found in Fig. 4c. This was because as the cycle progresses, H^+ is consumed in the electrolyte, and the pH gradually increases, triggering the deposition of additional Mn^{2+}, resulting in an increase in capacity.[39] Fig. 4d shows the rate capability of Cu–MnO_2 and δ-MnO_2 cathodes measured at a rate of 0.3–5 A g^{-1}. As the current density increased, the specific capacity of electrodes decreased due to the limitation of electrochemical reaction kinetics. The Cu–MnO_2 cathode exhibited a discharge capacity of 617.85, 487.36, 315.14, 130.64, and 87.33 mA h g^{-1} at a rate of 0.3, 0.5, 1, 3, and 5 A g^{-1}, respectively. After restoration to 0.3 A g^{-1}, the capacity of the Cu–MnO_2 cathode reached up to 506 mA h g^{-1}. In contrast, δ-MnO_2 exhibited much lower capacity than Cu–MnO_2 at the same rate. This finding suggested that the insertion of copper ions could modulate the electronic configuration and efficient ion/charge storage sites of δ-MnO_2 and, thus, improve the electron-transport and ion-diffusion capacities of the δ-MnO_2 cathode. The greater-than-theoretical-capacity of Cu–MnO_2 was due to the additional capacity provided by the 2 e^- deposition reaction of Mn^{2+} added in the electrolytic liquid.[39,40] To deeply research long-term cycling stability at high rates, Cu–MnO_2 and δ-MnO_2 cathodes were tested at a rate of 5 A g^{-1}. As shown in Fig. 4e, Cu–MnO_2 maintained a capacity of 114.23 mA h g^{-1} after 1500 cycles of 5 A g^{-1}, which was much higher than that of δ-MnO_2 (80.4 mA h g^{-1}). At the same time, Cu–MnO_2 could maintain a stable coulombic efficiency of nearly 100% under long cycles while δ-MnO_2 showed an unstable coulombic efficiency. These results showed that Cu^{2+} could be used as the pillars in the interlayer of Cu–MnO_2 to obtain excellent electrochemical properties compared with δ-MnO_2.[21,41] For a more comprehensive study of the electrochemical properties of Cu–MnO_2, we tested its performance in different electrolytes at a current density of 1 A g^{-1}. It can be seen from Fig. S6† that Cu–MnO_2 exhibited a relatively stable long cycle performance in different electrolytes, but its specific capacity was different in different electrolytes. In an aqueous electrolyte without Mn^{2+}, Cu–MnO_2 showed the highest electrochemical performance in 2 M $ZnSO_4$, but poor specific capacity in 3 M and 2 M $Zn(CF_3SO_3)_2$. This was because SO_4^- easily binds to H_2O and forms a water-rich layer around the cathode, which provides kinetic support for H^+ embedding, while $CF_3SO_3^-$ is hydrophobic and preferentially adsorbed at the cathode to create a low-water environment, which hinders H^+ embedding and results in reduced capacity.[42] In a non-aqueous point solution, DMSO electrolyte with 5% H_2O showed better electrochemical performance than that of pure DMSO. This was because the high electrostatic interaction within the ion pair ($Zn^{2+}/CF_3SO_3^-$) in DMSO and the high desolvation penalty at the electrode–electrolyte interface will reduce ion transport and increase the energy loss of the charge-storage reaction.[43] At the same time, the lack of H^+ in DMSO stops it providing capacity contribution, so it shows poor specific capacity. The addition of H_2O causes MnO_2 to adsorb water during the discharge process and form superhydrated zinc pyroxene, which greatly promotes the

diffusion of Zn^{2+} and improves the reactivity of the Zn-insertion reaction. In addition, we compared Cu–MnO_2 with other reported advanced ZIBs cathodes (Table S1†). Cu–MnO_2 showed better electrochemical properties than that of most cathodes.

In order to study how Cu^{2+} improves the electrochemical performance of δ-MnO_2, the ion diffusion kinetics and energy storage mechanism of the cathode were investigated by CV, galvanostatic intermittent titration technique (GITT) and electrochemical impedance spectroscopy (EIS). As shown in Fig. 5a, the CV curves of Cu–MnO_2 at different scanning rates were measured from 0.1 to 0.5 mV s^{-1}. Two pairs of redox peaks were detected during the scan, which corresponded to the reversible insertion–extraction of Zn^{2+}/H^+. Although polarization during the intercalation/deintercalation process led to a slight peak shift, the well-maintained shape of the CV curves indicated a reversible redox reaction of the Cu–MnO_2 cathode. The variation of peak current (i) with scan rate (v) follows an empirical power-law, which can be expressed by the following formula:[44]

$$i = av^b \quad (1)$$

where i denotes the current, v reflects the scan rate, and a and b are variable parameters. The fitted value of b represents the type of energy storage, when b = 0.5 indicates the diffusion-control process and b = 1 suggests the capacitive-storage process. The b values of P1, P2, P3 and P4 of Cu–MnO_2 were 0.7, 0.58, 0.51 and 0.83, respectively (Fig. 5b). These findings suggest that the electrochemical process of the Cu–MnO_2 cathode was controlled by diffusion and capacitance processes, and was principally controlled by capacitance. The contribution rates of capacitance control and diffusion control can be calculated by the following equation:[44]

$$i(v) = k_1v + k_2v^{1/2} \quad (2)$$

The response currents generated by capacitive and diffusion-controlled behaviour were calculated using k_1v and $k_2v^{1/2}$. As shown in Fig. 5c, at the scanning rates of 0.1, 0.2, 0.3, 0.4 and 0.5 mV s^{-1}, the capacitance contribution was 53.48%, 70.77%, 73.89%, 79.26% and 86.34%, respectively, indicating that capacitor control was dominant in Cu–MnO_2. However, the δ-MnO_2 cathode exhibited a lower capacitance ratio, as shown in Fig. S6,† indicating that Cu^{2+} could introduce more capacitance to promote the electrochemical performance of δ-MnO_2.

The ion diffusion coefficient was measured by constant current intermittent titration (GITT) and calculated according to the following formula:[45]

$$D = \frac{4}{\pi\tau}\left(\frac{m_B V_m}{M_B S}\right)^2\left(\frac{\Delta E_s}{\Delta E_t}\right)^2 \quad (3)$$

τ: constant current pulse duration
m_B: mass loading of the reactant
M_B: molecular volume
V_m: molar volume

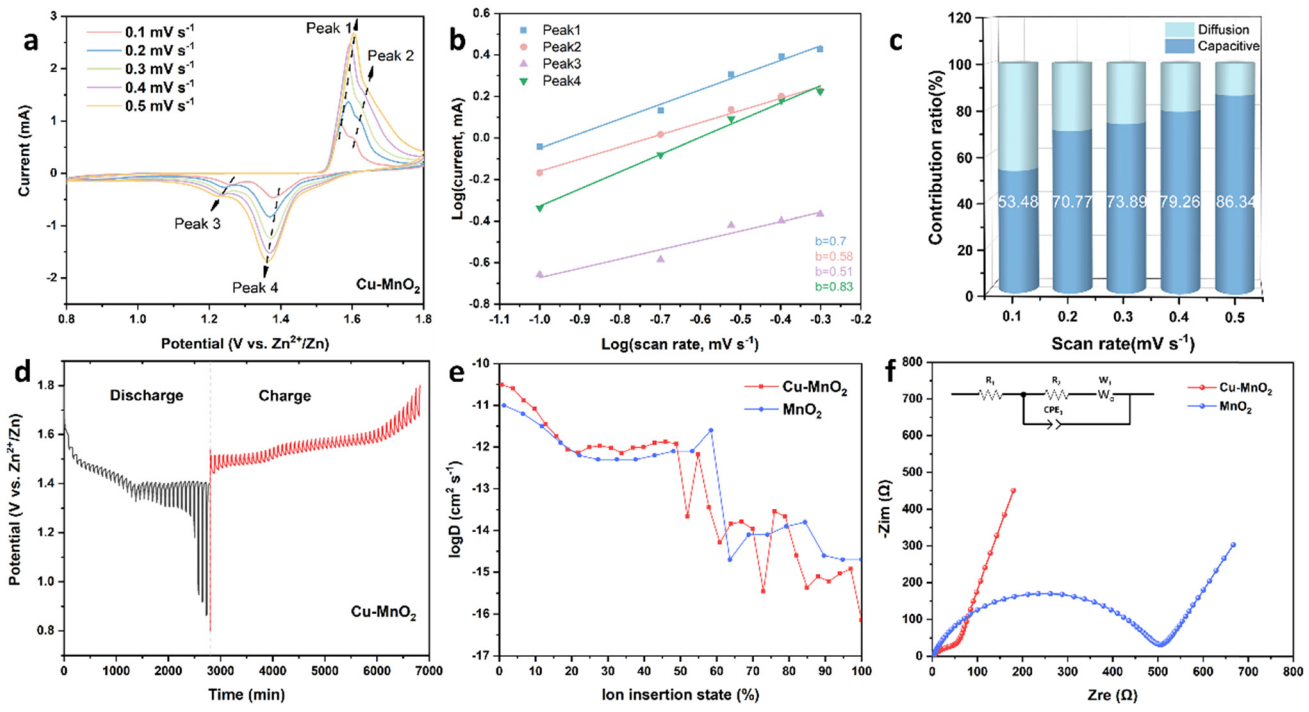

Fig. 5 (a) CV curves of 0.1–0.5 mV s^{-1}. (b) Corresponding dependence of log i *versus* log v at selected oxidation/reduction states. (c) Capacitive-controlled ratio at various scan rates. (d) GITT curves of Cu–MnO_2. (e) Diffusion coefficient of Cu–MnO_2 and δ-MnO_2. (f) EIS spectra.

S: electrode–electrolyte interface area
ΔE_s: change in steady-state voltage
ΔE_t: change in discharge/charge voltage

Fig. 5d and S7† are the GITT curves of Cu–MnO_2 and δ-MnO_2 cathodes. The appearance of the two platforms was caused by the sequential intercalation of H^+ and Zn^{2+}.[46,47] The ion diffusion coefficient (D) is shown in Fig. 5e. The diffusion coefficient before 50% was greater than the diffusion coefficient after 50%, which corresponded to the intercalation process of H^+ and Zn^{2+}, respectively. This observation indicated that the diffusion kinetics of H^+ and Zn^{2+} were different in the electrochemical process. Compared with δ-MnO_2, the H^+ diffusion coefficient of the Cu–MnO_2 cathode was one order of magnitude higher, indicating that the pre-intercalation of Cu^{2+} accelerated the diffusion rate of H^+, improved the electrochemical performance and enhanced the capacity of Cu–MnO_2. Fig. 5f shows the Nyquist plot of Cu–MnO_2 and δ-MnO_2 cathodes. The Rct (charge transfer impedance) of Cu–MnO_2 and δ-MnO_2 obtained by circuit fitting were 57.92 (Ω) and 505.04 (Ω), respectively, which further confirmed the improvement of the kinetics performance of δ-MnO_2 by Cu^{2+}.

To further investigate the ion-transfer behaviour and energy-storage mechanism of the Cu–MnO_2 cathode in AZIB, the crystal configuration, valence state and micromorphology of the cathode were studied by *ex situ* XRD, XPS and SEM. Fig. 6a and b show the XRD patterns of Cu–MnO_2 in different states during one cycle. When fully discharged (0.8 V), there were characteristic peaks at 34.6° and 58.69° which were attributed to Zn_2MnO_4 (JCPDS no. 19-1459). Diffraction peaks were observed at 28.14° and 32.8°, which corresponded to $Zn_4SO_4(OH)_6{\cdot}H_2O$ (ZSH) (JCPDS no. 39-0690), while the characteristic peak of MnOOH (JCPDS no. 24-0713) was observed at 21.13°. The formation of MnOOH and ZSH during discharge indicated that H^+ intercalated into δ-MnO_2. With more H^+ being consumed, a large amount of OH^- was produced in the electrolyte, and excess OH^-, Zn^{2+} and SO_4^{2-} reacted to obtain ZSH. The formation of Zn_2MnO_4 was due to the insertion of Zn^{2+} into the interlayer of δ-MnO_2. The shift of the characteristic peaks of δ-MnO_2 from 37.39° and 12.52° to 35.86° and 10.93° confirmed the behaviour of ion intercalation. In the process of charging, the characteristic peaks of MnOOH and ZSH gradually disappeared, which suggested the good cyclic reversibility of H^+. The characteristic peaks of Zn_2MnO_4 could still be observed when the charge was up to 1.8 V, indicating the poor reaction kinetics of Zn^{2+}. The process stated above suggested the reaction mechanism of H^+ and Zn^{2+} intercalation. The *ex situ* SEM results (Fig. 6c and f) showed that ZSH nanosheets were formed when discharged to 0.8 V, and disappeared when charged to 1.8 V, revealing the good reversibility of the microstructure. Fig. 6d and e show the *ex situ* XPS spectra of Mn 2p and O 1s at full charge (1.8 V) and complete discharge (0.8 V). When fully discharged (0.8 V), the peak area of Mn^{3+} increased significantly, further demonstrating the embedding of Zn^{2+} and H^+, and leading to the reduction of Mn^{4+} to Mn^{3+}. When fully charged (1.8 V), the content of Mn^{4+} increased, indicating that the deintercalation of ions re-oxidized Mn^{3+} to Mn^{4+}. The XPS spectrum of Zn 2p is shown in Fig. S8.† The peak of Zn 2p decreased when charging from 0.8 to 1.8 V, which indicated the deintercalation behaviour of Zn^{2+}. The observation of the peak of Zn at 1.8 V suggested

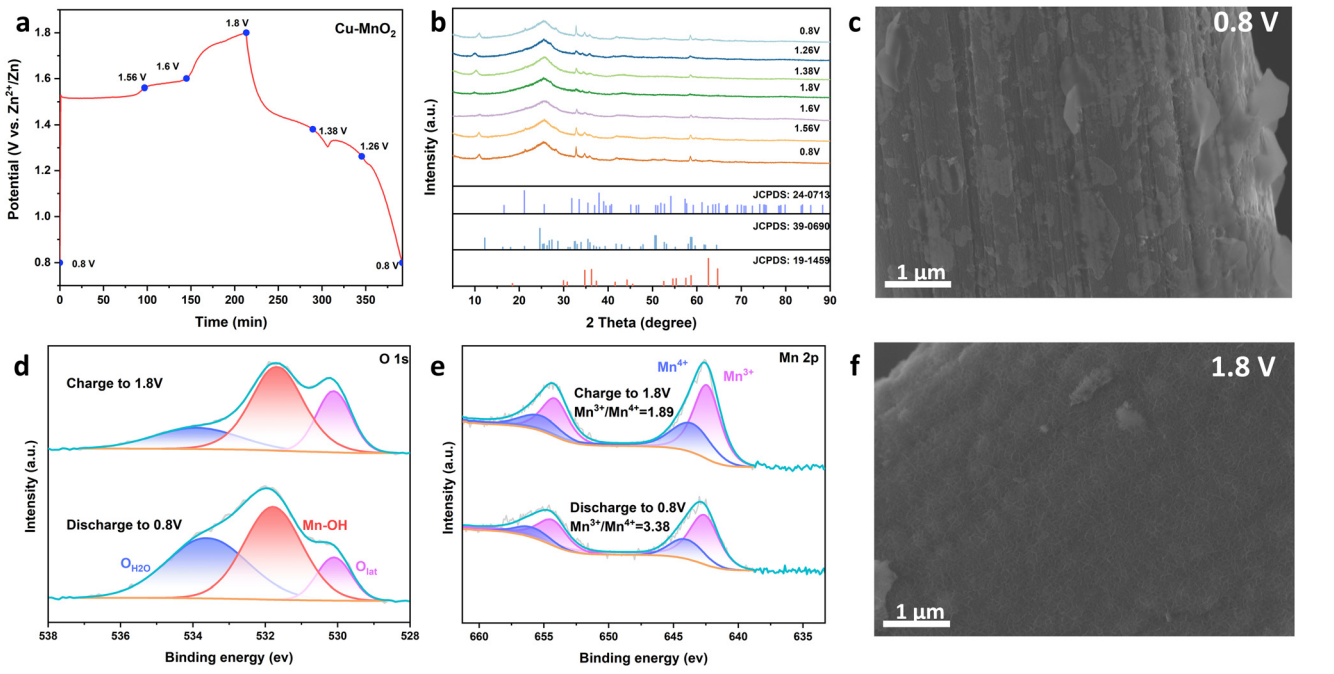

Fig. 6 (a) Typical cycle curves. (b) *Ex situ* XRD patterns at selected potentials. SEM images of (c) 0.8 V and (f) 1.8 V. XPS spectra of (d) O1s and (e) Mn2p.

that the Zn^{2+} mentioned above was not completely deintercalated, indicating the low diffusion kinetics of Zn^{2+}. In addition, Fig. 6d reveals the change of O valence state during charge and discharge. When discharging to 0.8 V, the peak area of O_{H_2O} was increased significantly due to the formation of ZSH, while the peak area of O_{lat} decreased due to the intercalation of ions. The opposite process during charging indicated that H^+ and Zn^{2+} left the lattice of Cu–MnO_2 and the large chunks of ZSH disappeared, which showed that Cu–MnO_2 had good reversibility. The above results showed that the Cu–MnO_2 cathode exhibited good cyclic reversibility, and it was a feasible strategy to improve the embedding and removal ability of H^+ by intercalation of Cu^{2+}. In addition, we studied the structural changes during the long-term cycling of the battery. As shown in Fig. S10a,† an obvious characteristic peak of ZSH appeared in the XRD curve of the electrode after 1500 cycles, indicating that irreversible phase transition occurred during the long cycle. As mentioned above, H^+ in the electrolyte was consumed during the electrochemical cycle, which led to an increase in pH and triggered ZSH deposition. The deposition of a large amount of ZSH would hinder the contact between Cu–MnO_2 and the electrolyte, resulting in a decrease in capacity. Fig. S10b† shows the SEM image of the electrode after 1500 C, and many ZSH patches in the figure confirm this interpretation.

3 Conclusions

Cu^{2+}-intercalated δ-MnO_2 (Cu–MnO_2) was grown *in situ* on a mesoporous CCs substrate by a hydrothermal method as the cathode of AZIB, and its electrochemical properties were investigated. The designed Cu–MnO_2 cathodes showed excellent specific capacity, rate performance and cycle stability in AZIB. Cu–MnO_2 exhibited a reversible capacity of 280 mA h g^{-1} at the rate of 1 A g^{-1}, maintained 93% capacity after 400 cycles, and had a high specific capacity of 114.23 mA h g^{-1} at 5 A g^{-1} after 1500 cycles. The combined use of CV, GITT, EIS, *ex situ* XRD and XPS showed that the intercalated Cu^{2+} formed a strong ionic bond with the oxygen atom, thus improving the stability of the layered structure and enhancing the H^+ transfer kinetics.

4 Experimental section

4.1 Chemicals and materials

PEO-5000, 2-bromoisobutyryl bromide, and *N*,*N*,*N*′,*N*′,*N*′-pentamethyldiethylenetriamine (PMDETA) were purchased from Aladdin. Tetrahydrofuran (THF) (>99%), pyridine (>99%), cuprous bromide (CuBr), ammonium hydroxide (NH_4OH, 28–30 wt%), dopamine hydrochloride, and copper(II) chloride dihydrate ($CuCl_2{\cdot}2H_2O$) were obtained from Greagent. Potassium permanganate ($KMnO_4$) and ethanol were sourced from Sinopharm Group Chemical Reagents. All reagents were of analytical grade and did not require further purification. Deionized water was used for all experiments.

4.2 Synthesis of Cu–MnO_2 and δ-MnO_2

Cu–MnO_2 and δ-MnO_2 was prepared by a one-step hydrothermal method. $KMnO_4$ and $CuCl_2{\cdot}2H_2O$ at a molar ratio of 10 : 1 were dissolved in 10 ml of water under vigorous stirring for 10 min. One piece of carbon cloth (2 × 2) was placed into the above solution, transferred into a Teflon™-lined stainless-steel autoclave and heated at 180 °C for 2 h. After cooling down to room temperature, the obtained sample was washed with DI water thrice, and dried using a vacuum oven at 60 °C for 12 h. δ-MnO_2 was synthesized using a similar procedure without $CuCl_2{\cdot}2H_2O$.

4.3 Materials characterization

The crystal structure of the sample was characterized by X-ray diffraction (XRD) using a D/Max-2550 PC diffractometer (Rigaku). The microstructure of electrodes was characterized by scanning electron microscopy (SEM) using the MAIA3 system (TESCAN) and transmission electron microscopy (TEM) employing a 2100F system (JEM). HAADF-STEM and EDS elemental mapping were done using a Talos F200S setup operating at 200 kV. Raman spectra were acquired using a reflex Raman microscope with laser excitation at 532 nm. N_2 sorption was carried out with an Autosorb-iQ system (Quantachrome) to measure the Brunauer–Emmett–Teller (BET) surface area and pore-size distribution. The BET method was employed for the determination of the specific surface area of catalysts. The Barrett–Joyner–Halenda (BJH) model was employed to analyze the pore-size distribution and pore volume. Electrode surface valence and chemical environment were investigated using an 250Xi setup (Escalab) equipped with Al Kα radiation.

4.4 Electrochemical measurements

Cu–MnO_2 was prepared on carbon cloth by *in situ* growth and used as the cathode (area: 0.25 cm^2) without conductive additives or adhesives. The mass loading of electrodes was 1.5 mg cm^{-2}. CR2032 coin cells were assembled in air. The configuration was with a zinc anode (diameter: 14 mm), glass fiber film (GF/D; Whatman), and 2 M $ZnSO_4$ and 0.2 M $MnSO_4$ as the electrolyte to estimate the properties of cathodic active materials. The galvanostatic discharge/charge (GCD) curve and GITT curve were created on the NEWARE battery test system, and the test voltage was 0.8–1.8 V. The specific capacity of the battery was calculated using this formula:

$$Q_s = \frac{I}{m}(\Delta t)$$

where Q_s represents the specific capacity (mA h g^{-1}), I represents the current (mA), m denotes the mass of the active substance (g) and Δt represents the discharge time.

The discharge GITT profiles were obtained at 0.1 A g^{-1} for 1200 s followed with a rest for 1 h. The CV curve and EIS curve were measured by an electrochemical workstation (CHI600E). The frequency range of EIS was 100 kHz to 0.01 Hz. All tests were performed at room temperature.

Author contributions

Conceptualization: P. Q., R. J. and Y. F. Methodology: P. Q., R. J., W. S. and Y. F. Validation: P. Q. and R. J. Data analysis, R. J. Investigation: R. J. Resources, P. Q. and W. L. Data curation: R. J., Y. Z., G. R., Y. W. and B. G. Writing (preparation of original draft): R. J., W. S. and P. Q. Writing (review and editing): P. Q., W. S. and R. J. Visualization: R. J. Supervision: P. Q. and W. L. Project administration: P. Q. and W. L. Funding acquisition: P. Q. and W. L.

Conflicts of interest

There are no conflicts of interest to declare.

Acknowledgements

This work was supported by the National Natural Science Foundation of China (52225204, 52173233, 52002059 and 52202085), Innovation Program of Shanghai Municipal Education Commission (2021-01-07-00-03-E00109), Natural Science Foundation of Shanghai (23ZR1479200), "Shuguang Program" supported by the Shanghai Education Development Foundation and Shanghai Municipal Education Commission (20SG33), DHU Distinguished Young Professor Program (LZA2022001 and LZB2023002) and the Fundamental Research Funds for Central Universities (2232023G-07, 2232024Y-01).

References

1 J. H. Lim, J. H. Won, M. K. Kim, D. S. Jung, M. Kim, C. Park, S.-M. Koo, J.-M. Oh, H. M. Jeong, H. Sohn and W. H. Shin, Synthesis of flower-like manganese oxide for accelerated surface redox reactions on nitrogen-rich graphene of fast charge transport for sustainable aqueous energy storage, *J. Mater. Chem. A*, 2022, **10**, 7668–7676.

2 S.-J. Tan, J. Yue, Z. Chen, X.-X. Feng, J. Zhang, Y.-X. Yin, L. Zhang, J.-C. Zheng, Y. Luo, S. Xin and Y.-G. Guo, Asymmetric fire-retardant quasi-solid electrolytes for safe and stable high-voltage lithium metal battery, *Energy Mater. Adv.*, 2024, **5**, 0076.

3 Z. Zheng, X. Zhong, Q. Zhang, M. Zhang, L. Dai, X. Xiao, J. Xu, M. Jiao, B. Wang, H. Li, Y. Jia, R. Mao and G. Zhou, An extended substrate screening strategy enabling a low lattice mismatch for highly reversible zinc anodes, *Nat. Commun.*, 2024, **15**, 753.

4 M. Fu, H. Yu, S. Huang, Q. Li, B. Qu, L. Zhou, G.-C. Kuang, Y. Chen and L. Chen, Building sustainable saturated fatty acid-zinc interfacial layer toward ultra-stable zinc metal anodes, *Nano Lett.*, 2023, **23**, 3573–3581.

5 H. Xia, W. Zhang, S. Cao and X. Chen, A figure of merit for fast-charging Li-ion battery materials, *ACS Nano*, 2022, **16**, 8525–8530.

6 L. Miao, R. Wang, W. Xin, L. Zhang, Y. Geng, H. Peng, Z. Yan, D. Jiang, Z. Qian and Z. Zhu, Three-functional ether-based co-solvents for suppressing water-induced parasitic reactions in aqueous Zn-ion batteries, *Energy Storage Mater.*, 2022, **49**, 445–453.

7 Z. Zhu, S. Cao, X. Ge, S. Xi, H. Xia, W. Zhang, Z. Lv, J. Wei and X. Chen, Enabling the high-voltage operation of layered ternary oxide cathodes via thermally tailored interphase, *Small Methods*, 2022, **6**, 2100920.

8 L. Ma, S. Chen, C. Long, X. Li, Y. Zhao, Z. Liu, Z. Huang, B. Dong, J. A. Zapien and C. Zhi, Achieving high-voltage and high-capacity aqueous rechargeable zinc ion battery by incorporating two-species redox reaction, *Adv. Energy Mater.*, 2019, **9**, 1902446.

9 F. Ming, Y. Zhu, G. Huang, A. H. Emwas, H. Liang, Y. Cui and H. N. Alshareef, Co-solvent electrolyte engineering for stable anode-free zinc metal batteries, *J. Am. Chem. Soc.*, 2022, **144**, 7160–7170.

10 D. Selvakumaran, A. Pan, S. Liang and G. Cao, A review on recent developments and challenges of cathode materials for rechargeable aqueous Zn-ion batteries, *J. Mater. Chem. A*, 2019, **7**, 18209–18236.

11 X. Jia, C. Liu, Z. G. Neale, J. Yang and G. Cao, Active materials for aqueous zinc ion batteries: Synthesis, crystal structure, morphology, and electrochemistry, *Chem. Rev.*, 2020, **120**, 7795–7866.

12 X. Ji and L. F. Nazar, Best practices for zinc metal batteries, *Nat. Sustain.*, 2024, **7**, 98–99.

13 S. Chang, J. F. F. Gomez, S. Katiyar, G. Morell and X. Wu, Trivalent indium metal as a high-capacity, high-efficiency, low-polarization, and long-cycling anode for aqueous batteries, *J. Am. Chem. Soc.*, 2023, **145**, 24746–24754.

14 Y. Zhu, G. Liang, X. Cui, X. Liu, H. Zhong, C. Zhi and Y. Yang, Engineering hosts for Zn anodes in aqueous Zn-ion batteries, *Energy Environ. Sci.*, 2024, **17**, 369–385.

15 X. Hu, G. Wang, J. Li, J. Huang, Y. Liu, G. Zhong, J. Yuan, H. Zhan and Z. Wen, Significant contribution of single atomic Mn implanted in carbon nanosheets to high-performance sodium-ion hybrid capacitors, *Energy Environ. Sci.*, 2021, **14**, 4564–4573.

16 S. Liu, L. Kang, J. M. Kim, Y. T. Chun, J. Zhang and S. C. Jun, Recent advances in vanadium-based aqueous rechargeable zinc-ion batteries, *Adv. Energy Mater.*, 2020, **10**, 2001769.

17 J. Zhao, Z. Xu, Z. Zhou, S. Xi, Y. Xia, Q. Zhang, L. Huang, L. Mei, Y. Jiang, J. Gao, Z. Zeng and C. Tan, A safe flexible self-powered wristband system by integrating defective MnO_{2-x} nanosheet-based zinc-ion batteries with perovskite solar cells, *ACS Nano*, 2021, **15**, 10597–10608.

18 J. Wang, J. G. Wang, H. Liu, C. Wei and F. Kang, Zinc ion stabilized MnO_2 nanospheres for high capacity and long lifespan aqueous zinc-ion batteries, *J. Mater. Chem. A*, 2019, **7**, 13727–13735.

19 T. Xiong, Y. Zhang, W. S. V. Lee and J. Xue, Defect engineering in manganese-based oxides for aqueous rechargeable zinc-ion batteries: A review, *Adv. Energy Mater.*, 2020, **10**, 2001769.

20 X. Zhu, Z. Cao, W. Wang, H. Li, J. Dong, S. Gao, D. Xu, L. Li, J. Shen and M. Ye, Superior-performance aqueous zinc-ion batteries based on the In Situ growth of MnO_2 nanosheets on V_2CT_X MXene, *ACS Nano*, 2021, **15**, 2971–2983.

21 F. Jing, Y. Liu, Y. Shang, C. Lv, L. Xu, J. Pei, J. Liu, G. Chen and C. Yan, Dual ions intercalation drives high-performance aqueous Zn-ion storage on birnessite-type manganese oxides cathode, *Energy Storage Mater.*, 2022, **49**, 164–171.

22 Y. Zhao, S. Zhang, Y. Zhang, J. Liang, L. Ren, H. J. Fan, W. Liu and X. Sun, Vacancy-rich Al-doped MnO_2 cathodes break the trade-off between kinetics and stability for high-performance aqueous Zn-ion batteries, *Energy Environ. Sci.*, 2024, **17**, 1279–1290.

23 H. Tang, W. Chen, N. Li, Z. Hu, L. Xiao, Y. Xie, L. Xi, L. Ni and Y. Zhu, Layered MnO_2 nanodots as high-rate and stable cathode materials for aqueous zinc-ion storage, *Energy Storage Mater.*, 2022, **48**, 335–343.

24 X. Xiao, L. Zhang, W. Xin, M. Yang, Y. Geng, M. Niu, H. Zhang and Z. Zhu, Self-assembled layer of organic phosphonic acid enables highly stable MnO_2 cathode for aqueous znic batteries, *Small*, 2024, 2309271.

25 A. Zhang, R. Zhao, Y. Wang, J. Yue, J. Yang, X. Wang, C. Wu and Y. Bai, Hybrid superlattice-triggered selective proton Grotthuss intercalation in δ-MnO_2 for high-performance zinc-ion battery, *Angew. Chem., Int. Ed.*, 2023, **62**, e202313163.

26 P. Qiu, Y. Yao, W. Li, Y. Sun, Z. Jiang, B. Mei, L. Gu, Q. Zhang, T. Shang, X. Yu, J. Yang, Y. Fang, G. Zhu, Z. Zhang, X. Zhu, T. Zhao, W. Jiang, Y. Fan, L. Wang, B. Ma, L. Liu, Y. Yu and W. Luo, Sub-nanometric manganous oxide clusters in nitrogen doped mesoporous carbon nanosheets for high-performance lithium–sulfur batteries, *Nano Lett.*, 2021, **21**, 700–708.

27 H. Yao, H. Yu, Y. Zheng, N. W. Li, S. Li, D. Luan, X. W. Lou and L. Yu, Pre-intercalation of ammonium ions in layered δ-MnO_2 nanosheets for high-performance aqueous zinc-ion batteries, *Angew. Chem., Int. Ed.*, 2023, **62**, e202315257.

28 J. Zhang, W. Li, J. Wang, X. Pu, G. Zhang, S. Wang, N. Wang and X. Li, Engineering p-band center of oxygen boosting H^+ intercalation in δ-MnO_2 for aqueous zinc ion batteries, *Angew. Chem., Int. Ed.*, 2023, **62**, e202215654.

29 G. Wang, Y. Wang, B. Guan, J. Liu, Y. Zhang, X. Shi, C. Tang, G. Li, Y. Li, X. Wang and L. Li, Hierarchical K-birnessite-MnO_2 carbon framework for high-energy-density and durable aqueous zinc-ion battery, *Small*, 2021, **17**, 2104557.

30 R. Cao, P. Zhang, Y. Liu and X. Zheng, Ammonium-treated birnessite-type MnO_2 to increase oxygen vacancies and surface acidity for stably decomposing ozone in humid condition, *Appl. Surf. Sci.*, 2019, **495**, 143607.

31 M. Ju, Z. Chen, H. Zhu, R. Cai, Z. Lin, Y. Chen, Y. Wang, J. Gao, X. Long and S. Yang, Fe(III) docking-activated sites in layered birnessite for efficient water oxidation, *J. Am. Chem. Soc.*, 2023, **145**, 11215–11226.

32 F. Wei, T. Zhang, R. Dong, Y. Wu, W. Li, J. Fu, C. Jing, J. Cheng, X. Feng and S. Liu, Solution-based self-assembly synthesis of two-dimensional-ordered mesoporous conducting polymer nanosheets with versatile properties, *Nat. Protoc.*, 2023, **18**, 2459–2484.

33 J. Li, R. Li, W. Wang, K. Lan and D. Zhao, Ordered mesoporous crystalline frameworks toward promising energy applications, *Adv. Mater.*, 2024, **36**, 2311460.

34 T. Sun, Q. Nian, S. Zheng, J. Shi and Z. Tao, Layered $Ca_{0.28}MnO_2{\cdot}0.5H_2O$ as a high performance cathode for aqueous zinc-ion battery, *Small*, 2020, **16**, 2000597.

35 G. Zhu, W. Zhu, Y. Lou, J. Ma, W. Yao, R. Zong and Y. Zhu, Encapsulate α-MnO_2 nanofiber within graphene layer to tune surface electronic structure for efficient ozone decomposition, *Nat. Commun.*, 2021, **12**, 4152.

36 H. Wang, R. Guo, H. Li, J. Wang, C. Du, X. Wang and Z. Zheng, 2D metal patterns transformed from 3D printed stamps for flexible Zn//MnO_2 in-plane micro-batteries, *Chem. Eng. J.*, 2022, **429**, 132196.

37 W. Ma, K. W. Kwan, R. Wu and A. H. W. Ngan, High-performing, linearly controllable electrochemical actuation of c-disordered δ-MnO_2/Ni actuators, *J. Mater. Chem. A*, 2021, **9**, 6261–6273.

38 C. Li, R. Kingsbury, A. S. Thind, A. Shyamsunder, T. T. Fister, R. F. Klie, K. A. Persson and L. F. Nazar, Enabling selective zinc-ion intercalation by a eutectic electrolyte for practical anodeless zinc batteries, *Nat. Commun.*, 2023, **14**, 3067.

39 H. Yang, T. Zhang, D. Chen, Y. Tan, W. Zhou, L. Li, W. Li, G. Li, W. Han, H. J. Fan and D. Chao, Protocol in evaluating capacity of Zn–Mn aqueous batteries: A clue of pH, *Adv. Mater.*, 2023, **35**, 2300053.

40 J. Huang, J. Zeng, K. Zhu, R. Zhang and J. Liu, High-performance aqueous zinc–manganese battery with reversible Mn^{2+}/Mn^{4+} double redox achieved by carbon coated MnO_x nanoparticles, *Nano-Micro Lett.*, 2020, **12**, 110.

41 K. Ma, Q. Li, C. Hong, G. Yang and C. Wang, Bi doping-enhanced reversible-phase transition of α-MnO_2 raising the cycle capability of Aqueous Zn–Mn batteries, *ACS Appl. Mater. Interfaces*, 2021, **13**, 55208–55217.

42 O. Zhanadilov, H. J. Kim, A. Konarov, J. Jeong, J.-H. Park, K. Y. Chung, Z. Bakenov, H. Yashiro and S.-T. Myung, Layered manganese oxide cathode boosting high-capacity and long-term cyclability in aqueous Zinc-Ion batteries, *Energy Storage Mater.*, 2024, **67**, 103283.

43 W. Kao-ian, J. Sangsawang, P. Kidkhunthod, S. Wannapaiboon, M. Suttipong, A. Khampunbut, P. Pattananuwat, M. T. Nguyen, T. Yonezawa and S. Kheawhom, Unveiling the role of water in enhancing the performance of zinc-ion batteries using dimethyl sulfoxide electrolyte and the manganese dioxide cathode, *J. Mater. Chem. A*, 2023, **11**, 10584–10595.

44 X.-Z. Zhai, J. Qu, J. Wang, W. Chang, H.-J. Liu, Y.-H. Liu, H. Yuan, X. Li and Z.-Z. Yu, Diffusion-driven fabrication of yolk-shell structured K-birnessite@mesoporous carbon

nanospheres with rich oxygen vacancies for high-energy and high-power zinc-ion batteries, *Energy Storage Mater.*, 2021, **42**, 753–763.

45 N. Zhang, M. Jia, Y. Dong, Y. Wang, J. Xu, Y. Liu, L. Jiao and F. Cheng, Hydrated layered vanadium oxide as a highly reversible cathode for rechargeable aqueous zinc batteries, *Adv. Funct. Mater.*, 2019, **29**, 1807331.

46 J. Wang, J.-G. Wang, H. Liu, Z. You, Z. Li, F. Kang and B. Wei, A highly flexible and lightweight MnO_2/graphene membrane for superior zinc-ion batteries, *Adv. Funct. Mater.*, 2021, **31**, 2007397.

47 D. Wang, L. Wang, G. Liang, H. Li, Z. Liu, Z. Tang, J. Liang and C. Zhi, A superior δ-MnO_2 cathode and a self-healing Zn-δ-MnO_2 battery, *ACS Nano*, 2019, **13**, 10643–10652.